# Minimum Trim Drag for a Three-Surface Supersonic Transport Aircraft

Sabet Seraj* and Joaquim R. R. A. Martins†
*University of Michigan, Ann Arbor, Michigan 48109*

**Three-surface configurations offer theoretical drag benefits over two-surface configurations, but the literature is unclear on what is the best configuration for a supersonic aircraft. This work uses trim-constrained drag minimization to compare the trim drag for three-surface, canard, and conventional variants of a supersonic transport aircraft. We first use RANS-based optimization to determine the minimum trim drag for a fixed planform geometry at a subsonic takeoff condition and a supersonic cruise condition. The three-surface configuration has the lowest trim drag at the supersonic condition. The canard and three-surface configurations have comparable trim drag at the subsonic condition. We then construct a supersonic buildup model to study the effects of variable trim surface sizing. When the trim surface spans are included as design variables, the design for minimum supersonic drag has practically no tail and a canard sized at 36% of the wing half-span. These results suggest that a canard configuration is best for supersonic trim drag.**

## I. Introduction

Three-surface aircraft have a theoretical advantage over canard and conventional two-surface configurations because three lifting surfaces allow for the aircraft to achieve minimum induced drag for any center of gravity location [1]. However, practical considerations have limited the use of three-surface configurations for subsonic aircraft. Kroo [2] used a linear vortex-based method and an analytic viscous drag model to determine that three-surface designs offer no obvious benefits over conventional configurations for subsonic aircraft. Selberg and Rokhsaz [3, 4] used a vortex lattice method to study trim for a general aviation aircraft and found that a three-surface configuration achieves a trimmed lift-to-drag ratio that is higher than a canard configuration but lower than a conventional configuration.

Different trim configurations have also been studied for supersonic aircraft. Lacey [5] conducted wind tunnel tests on a fighter-type aircraft with different trim surface geometries. They found that the three-surface configuration has lower drag at high angles of attack but that a conventional configuration is more effective at lower angles. Agnew and Hess Jr. [6] also ran wind tunnel tests on a three-surface and conventional fighter aircraft and found that the three-surface design was preferable for maneuverability and trim drag at Mach 0.9. In supersonic wind tunnel tests, Covell [7] found that a conventional fighter configuration has lower trim drag than a canard configuration. They also found that a linear aerodynamic model was unable to accurately compare canard, conventional, and tailless configurations at supersonic speeds. Finally, the Concorde was a tailless supersonic transport (SST) configuration that moved fuel to shift the center of gravity for trim [8]. This reduced trim drag in exchange for the added weight of the fuel transfer system.

There are two main contributions of this work. The first is studying different trim configurations for an SST rather than a fighter-type aircraft. The second is using nonlinear aerodynamic models for trim analysis and optimization. We determine the minimum trim drag for three-surface, canard, and conventional configurations with fixed trim surface sizing using the Reynolds-averaged Navier–Stokes (RANS) equations in Sec. II. We then formulate a supersonic buildup model to optimize the aircraft with trim surface sizing variables in Sec. III. The design space for this optimization includes the option to remove either trim surface and consequently achieve the best tradeoff between parasite and induced drag.

*Ph.D. Candidate, Department of Aerospace Engineering. Student Member AIAA.
†Pauline M. Sherman Collegiate Professor, Department of Aerospace Engineering. Fellow AIAA.

## II. RANS-based trim optimization

### A. Aircraft geometry and flight conditions

We first use RANS-based optimization to study trim for a constant geometry. The aircraft configuration we study is the UW-S-20A model developed by Nelson et al. [9], but without the nacelles (Fig. 1a). This aircraft is an SST with a cranked-arrow wing, a T-tail, and a canard. We use overset structured meshes to model the geometry in our RANS solver. One advantage of using overset meshes is that we can easily remove mesh blocks from the three-surface configuration to create meshes for canard, conventional, and trimless versions of the aircraft (Fig. 1). Some important dimensions are listed in Table 1. The pitching moment reference point is assumed to be fixed at 25% of the mean aerodynamic chord.

We consider two flight conditions for the RANS-based optimizations (Table 2). These flight conditions are based on flight envelopes and weight estimates from previous SST studies [10, 11]. The lift coefficient is computed from the takeoff weight for the subsonic condition and the midcruise weight for the supersonic condition.

**Table 1 Aircraft dimensions**

| Quantity | Value |
|---|---|
| Wing reference area ($S_{\text{ref}}$) | 373.03 m$^2$ |
| Wing mean aerodynamic chord ($\bar{c}$) | 14.565 m |
| Wing half-span | 14.760 m |
| Canard half-span | 2.327 m |
| Tail half-span | 5.543 m |

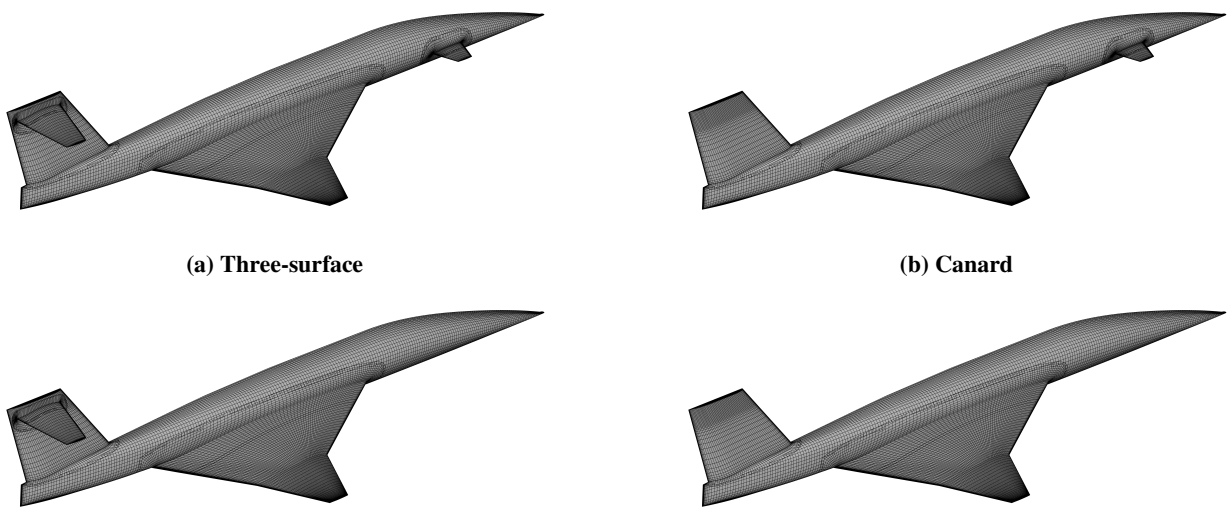

**(a) Three-surface** **(b) Canard**

**(c) Conventional** **(d) Trimless**

**Fig. 1 Overset configuration meshes**

**Table 2 Flight conditions**

| | Mach | Altitude, m | Altitude, ft | Reynolds | $C_L^*$ | $\alpha_{\min}$ | $\alpha_{\max}$ |
|---|---|---|---|---|---|---|---|
| Subsonic | 0.3 | 0 | 0 | $101.8 \times 10^6$ | 0.6933 | $-5°$ | $20°$ |
| Supersonic | 1.8 | 16,764 | 55,000 | $80.4 \times 10^6$ | 0.1665 | $-3°$ | $5°$ |

### B. RANS-based optimization setup

We use the MACH-Aero framework [12] for the RANS-based optimizations. We use ADflow [13] to solve the compressible RANS equations with the Spalart–Allmaras (SA) turbulence model [14] on overset structured meshes. The surface mesh that represents the geometry is modified using a combination of inverse-distance surface mesh deformation near component intersections [15] and free-form deformation [16, 17] away from the intersections. The surface mesh changes are propagated to the volume mesh using an inverse-distance deformation method [18, 19]. To run the optimizations, we use the SNOPT optimizer [20] through the interface provided by pyOptSparse [21]. The gradients are computed using the adjoint method [22].

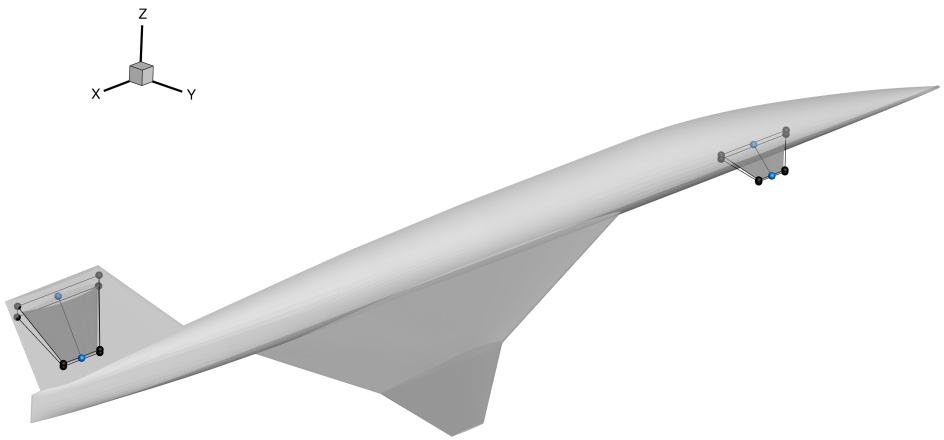


**Fig. 2 The trim surfaces can rotate about their 50% chord axis**

The optimization formulation for the trim-constrained drag minimization is shown in Table 3. The canard and tail rotation design variables are defined about the 50% chord axis of the canard and horizontal stabilizer, respectively. Figure 2 shows the FFD control points (black) and the reference axis control points (blue) that are used to define the rotations. The trim surface rotation bounds are based on the maximum rotation that produces a valid mesh. More details on the geometry parameterization for this SST configuration are provided by Seraj and Martins [23].

**Table 3 RANS-based trim drag minimization problem**

| | | Lower | Upper | Scaling |
|---|---|---|---|---|
| Minimize | $C_D$ | | | 100 |
| With respect to | Angle of attack | $\alpha_{\min}$ | $\alpha_{\max}$ | 0.1 |
| | Canard rotation | $-5°$ | $13°$ | 0.1 |
| | Tail rotation | $-9°$ | $9°$ | 0.1 |
| Subject to | $C_L \div C_L^*$ | 1 | 1 | 1 |
| | $C_M$ | 0 | 0 | 1 |

### C. RANS-based optimization results

The optimizations for the three-surface, canard, and conventional configurations at subsonic and supersonic speeds are shown in Table 4. The constraint violation for these optimizations is $2.0 \times 10^{-6}$ or lower, and the optimality is $3.9 \times 10^{-6}$ or lower. At the subsonic takeoff condition, the three-surface and canard configurations perform comparably.

The conventional configuration has 11.2% higher drag than the three-surface configuration. This is consistent with the experimental studies by Lacey [5] that showed that canards are more effective at subsonic speeds and high angles of attack. At the supersonic cruise condition, the conventional configuration has 9.4% higher drag than the three-surface configuration. The supersonic canard case is infeasible because of the upper bound on the canard rotation. We show in Sec. III.C that trimming with just the canard is feasible with larger rotations but incurs a large drag penalty. These results show that for the given trim surface sizing, the three-surface design performs better than the canard and conventional designs.

**Table 4 Trim optimization results**

| | Three-surface | Canard | Conventional |
|---|---|---|---|
| *Subsonic RANS* | | | |
| Drag counts | 1576 | 1569 | 1752 |
| Angle of attack | 12.4° | 12.2° | 13.8° |
| Canard rotation | 3.05° | 6.24° | – |
| Tail rotation | 0.42° | – | −4.95° |
| *Supersonic RANS* | | | |
| Drag counts | 330.1 | – | 361.2 |
| Angle of attack | 3.14° | – | 3.60° |
| Canard rotation | 7.62° | – | – |
| Tail rotation | −4.36° | – | −8.87° |
| *Supersonic Buildup* | | | |
| Drag counts | 329.9 | 450.9 | 368.2 |
| Angle of attack | 3.21° | 2.68° | 3.59° |
| Canard rotation | 8.13° | 20.1° | – |
| Tail rotation | −4.70° | – | −8.40° |

# III. Buildup-based trim optimization

## A. Supersonic buildup model

One disadvantage of optimizations that rely on mesh deformation is that the design space is limited to geometries that produce a valid mesh. To avoid this limitation, we construct a buildup model that uses a combination of RANS data and analytic functions. We start with running RANS on the trimless configuration at angles of attack from -6 to 6 deg. We then construct a quartic least-squares fit on the lift, drag, and moment curves. The trim surfaces and the interactions between components are modeled analytically based primarily on the approach presented by Raymer [24]. However, we use RANS simulations to inform some aspects of the analytic equations. We simulate the canard (Fig. 3a) and the horizontal stabilizer (Fig. 3b) at angles of attack from 0 to 50 deg at 5 deg increments. This gives us data to ensure that the analytic equations correctly model the nonlinear aerodynamics and that the model is applicable for trim surfaces with different aspect ratios.

### *1. Trim surface lift*

We model the trim surface lift as a cubic function:

$$C_L = C_{L_0} + C_{L_{\alpha=0}}\alpha - \frac{C_{L_{\alpha=0}}}{3\alpha_{L_{\max}}^2}\alpha^3, \tag{1}$$

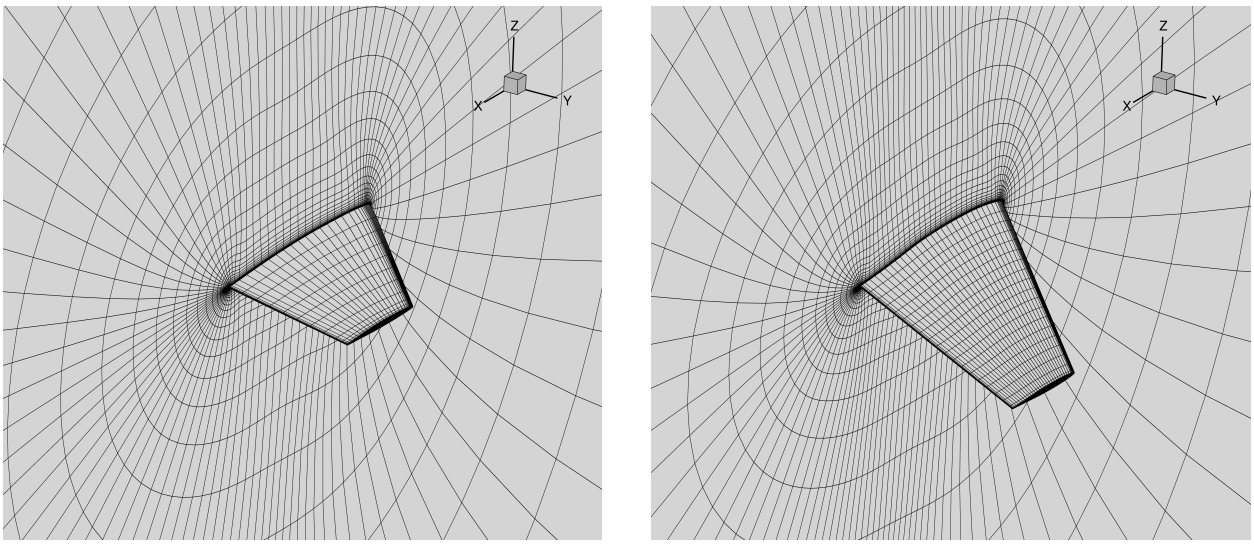


**(a) Canard (154,368 cells)** **(b) Horizontal stabilizer (211,136 cells)**

**Fig. 3 Trim surface meshes**

where $C_{L_{\alpha=0}}$ is the lift curve slope at zero angle of attack, and the coefficient for the cubic term is set such that the lift is maximized at $\alpha_{L_{\max}}$. We set $\alpha_{L_{\max}}$ to 40 deg based on the RANS simulations. The trim surfaces are approximately symmetric, so we assume $C_{L_0} = 0$. The ideal lift curve slope for a supersonic lifting surface is [24, Eq. 12.12]

$$C_{L_\alpha} = \frac{4}{\sqrt{M^2 - 1}}. \tag{2}$$

We apply a slight correction to the lift slope based on the aspect ratio:

$$C_{L_{\alpha=0}} = \frac{4}{(1 + A/8)\sqrt{M^2 - 1}}. \tag{3}$$

This nonlinear lift model results in good agreement with the RANS simulations (Fig. 4) for the canard ($A = 0.93$) and the horizontal stabilizer ($A = 1.49$). This model is also easy to differentiate to get the lift curve slope used in the drag and downwash computations. The nonlinear lift curve slope is

$$C_{L_\alpha} = C_{L_{\alpha=0}} - \frac{C_{L_{\alpha=0}}}{\alpha^2_{L_{\max}}}\alpha^2. \tag{4}$$

*2. Trim surface drag*

The trim surface drag consists of skin friction drag, wave drag, and induced drag. We compute the turbulent skin friction as [24, Eq. 12.27]

$$C_f = \frac{0.455}{(\log_{10} R)^{2.58}(1 + 0.144M^2)^{0.65}}. \tag{5}$$

The wave drag is [24, pp. 448-449]

$$C_{D_{\text{wave}}} = \frac{E_{\text{WD}}}{S_{\text{comp}}}\left(1 - 0.2(M - 1.2)^{0.57}\left(1 - \frac{\pi\Lambda^{0.77}_{\text{LE–deg}}}{100}\right)\right)(D/q)_{\text{SH}}, \tag{6}$$

where $E_{\text{WD}}$ is a wave drag efficiency factor, $\Lambda_{\text{LE–deg}}$ is the leading-edge sweep in degrees, and $(D/q)_{\text{SH}}$ is the drag for an equivalent Sears–Haack body. The Sears–Haack drag is computed as [24, Eq. 12.44]

$$(D/q)_{\text{SH}} = \frac{9\pi}{2}\left(\frac{A_{\max}}{\ell}\right)^2, \tag{7}$$

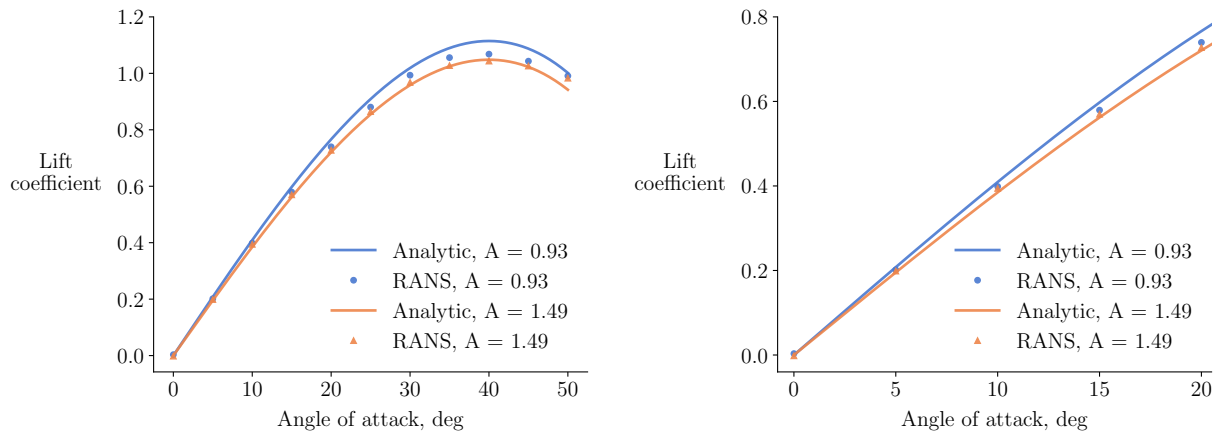


**(a) Full angle sweep** **(b) Zoom in on low angles**

**Fig. 4 Analytic lift compared to RANS**

where $A_{\max}$ is the maximum cross-sectional area and $\ell$ is the body length. We use the frontal area of the trim surface as the maximum cross-sectional area and the distance from the root leading edge to the tip trailing edge as the body length. We use $E_{\text{WD}} = 1.1$ to match the zero-lift drag from RANS. The zero-lift drag is the sum of the skin friction drag and wave drag:

$$C_{D_0} = C_f \frac{S_{\text{wet}}}{S_{\text{comp}}} + C_{D_{\text{wave}}}, \tag{8}$$

where the skin friction drag scales with the wetted area $S_{\text{wet}}$. We compute the induced drag with the leading-edge suction method [24, Eq. 12.56]:

$$C_{D_i} = \frac{C_L^2}{C_{L_\alpha}}. \tag{9}$$

The total drag is

$$C_D = C_{D_0} + C_{D_i}. \tag{10}$$

The drag buildup described above works well for low angles of attack (Fig. 5b), but it does not model the increase in drag that occurs once the lifting surface begins to stall at higher angles of attack. To account for stall effects, we use the model developed by Tangler and Ostowari [25]. This model was originally created for wind turbine design, but it has also been applied to subsonic aircraft design [26]. We show that the model is also useful for supersonic aircraft. The poststall drag is given by

$$C_D = B_1 \sin\alpha + B_2 \cos\alpha, \tag{11}$$

where

$$B_1 = C_{D_{\max}} \tag{12}$$

and

$$B_2 = C_{D_s} - B_1 \frac{\sin\alpha_s}{\cos\alpha_s}. \tag{13}$$

This model requires setting values for $C_{D_{\max}}$ and $\alpha_s$, the stall angle of attack. $C_{D_s}$ is the drag at the stall angle of attack computed using the prestall model. We find that using $C_{D_{\max}} = 2$ and a stall angle of attack of 22.5 deg results in good agreement between the drag buildup and RANS at high angles of attack (Fig. 5a). The poststall drag is only weakly dependent on the aspect ratio for the geometries we study, so an aspect ratio correction is not included in the poststall model. We use the Kreisselmeier–Steinhauser function [27] to smoothly transition from the prestall model to the poststall model. This approach was also used by Chauhan and Martins [26].

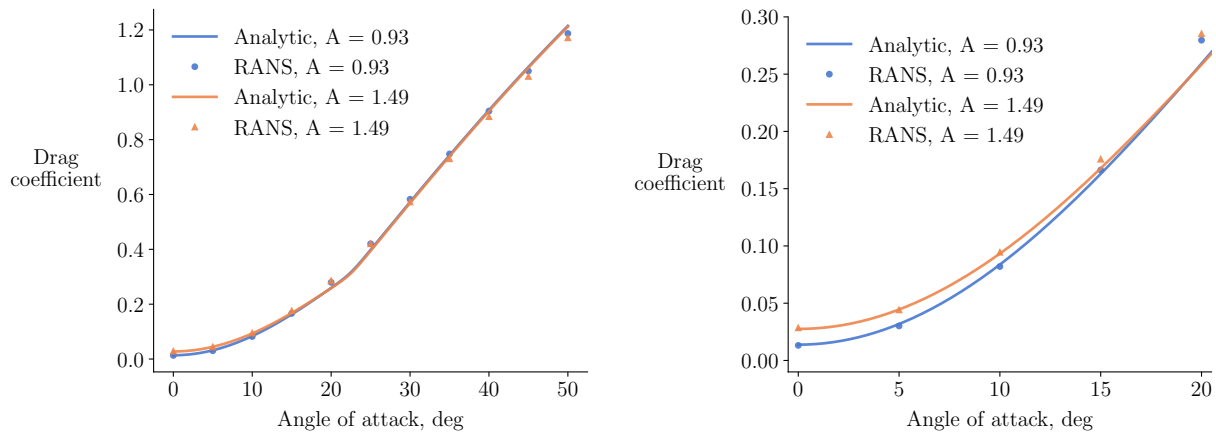


**(a) Full angle sweep** **(b) Zoom in on low angles**

**Fig. 5 Analytic drag compared to RANS**

*3. Downwash*

Accounting for downwash is critical for accurate buildup results. To simplify the downwash computation, we assume that the trimless part of the aircraft is entirely downstream of the canard and entirely upstream of the horizontal stabilizer. We account for the canard downwash on the trimless configuration and the trimless downwash on the horizontal stabilizer. The downwash derivative for an upstream component is computed as [24, Eq. 16.21b]

$$\left(\frac{\partial \epsilon}{\partial \alpha}\right)_{\text{upstream}} = \left(\frac{1.62 C_{L_\alpha}}{\pi A}\right)_{\text{upstream}}. \tag{14}$$

A component's total angle of attack is then computed as [24, Eq. 16.24]

$$\alpha_{\text{comp}} = \left(\alpha + i_{\text{upstream}}\right)\left(1 - \left(\frac{\partial \epsilon}{\partial \alpha}\right)_{\text{upstream}}\right) + i_{\text{comp}} - i_{\text{upstream}}, \tag{15}$$

where $i_{\text{comp}}$ is the component's incidence angle and $i_{\text{upstream}}$ is the upstream component's incidence angle.

*4. Total forces and pitching moment*

Finally, we combine the forces and moments from the trim surfaces and the trimless configuration. The lift is computed by adding all the component lift forces normalized using the wing reference area:

$$C_L = C_{L_{\text{trimless}}} + \sum_{\text{comp}} C_{L_{\text{comp}}} \frac{S_{\text{comp}}}{S_{\text{ref}}}. \tag{16}$$

The drag is computed in the same manner. The total moment is

$$C_M = C_{M_{\text{trimless}}} + \sum_{\text{comp}} \left( C_{N_{\text{comp}}} \frac{S_{\text{comp}}}{S_{\text{ref}}} \frac{\Delta x_{\text{comp}}}{\bar{c}} + C_{A_{\text{comp}}} \frac{S_{\text{comp}}}{S_{\text{ref}}} \frac{\Delta z_{\text{comp}}}{\bar{c}} \right), \tag{17}$$

where the normal force coefficient is

$$C_{N_{\text{comp}}} = C_{L_{\text{comp}}} \cos\alpha + C_{D_{\text{comp}}} \sin\alpha, \tag{18}$$

the axial force coefficient is

$$C_{A_{\text{comp}}} = -C_{L_{\text{comp}}} \sin\alpha + C_{D_{\text{comp}}} \cos\alpha, \tag{19}$$

$\Delta x_{\text{comp}}$ is the $x$-component of the vector from the moment reference point to the component's aerodynamic center, $\Delta z_{\text{comp}}$ is the $z$-component of the vector from the moment reference point to the component's aerodynamic center. We neglect the moments on the trim surfaces because these are much smaller than the trim surface forces multiplied by the moment arms.

*5. Model verification*

We verify the buildup model by comparing the buildup results to RANS. We first compare the buildup to RANS on the three-surface configuration at angles of attack from -6 to 6 deg (Fig. 6). The buildup drag matches RANS well but slightly underpredicts drag at higher angles of attack and negative angles of attack. The buildup lift and moment match RANS well at positive angles of attack but are only slightly better than the trimless configuration at negative angles of attack. The trim condition for the aircraft occurs at a low positive angle of attack, so we expect the buildup to perform well despite the discrepancies at negative angles.

Next, we look at the incremental changes in the aerodynamic coefficients for tail rotations (Fig. 8) and canard rotations (Fig. 7) at zero angle of attack. The buildup does not precisely match the RANS increments, but the trends are correct. In particular, the buildup has a negative lift increment for a positive canard deflection (Fig. 7b), which is the result of including the canard downwash effect on the trimless configuration. The tail rotation increments match RANS more closely than the canard rotation increments. This suggests that the canard's interaction with the fuselage and wing is more complex than interactions involving the tail.

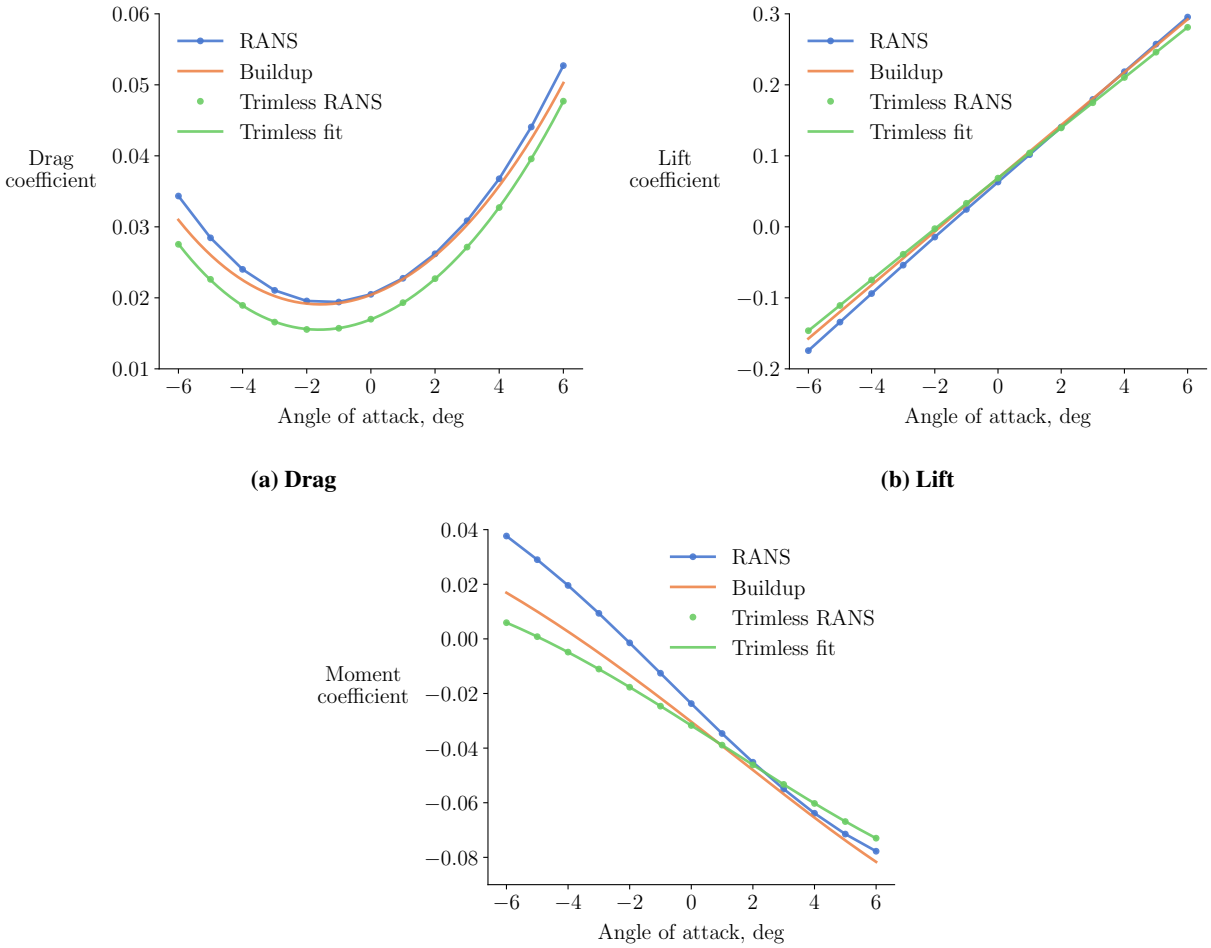


**(a) Drag**

**(b) Lift**

**(c) Pitching moment**

**Fig. 6 Angle of attack sweep**

## B. Buildup-based optimization setup

We wrap the buildup model in OpenMDAO [28] to facilitate optimization. As with the RANS-based optimizations, we use SNOPT through pyOptSparse as the optimizer. The gradients are computed using the complex-step method [29]. We consider optimizations with and without trim surface sizing. The optimization formulation with trim surface

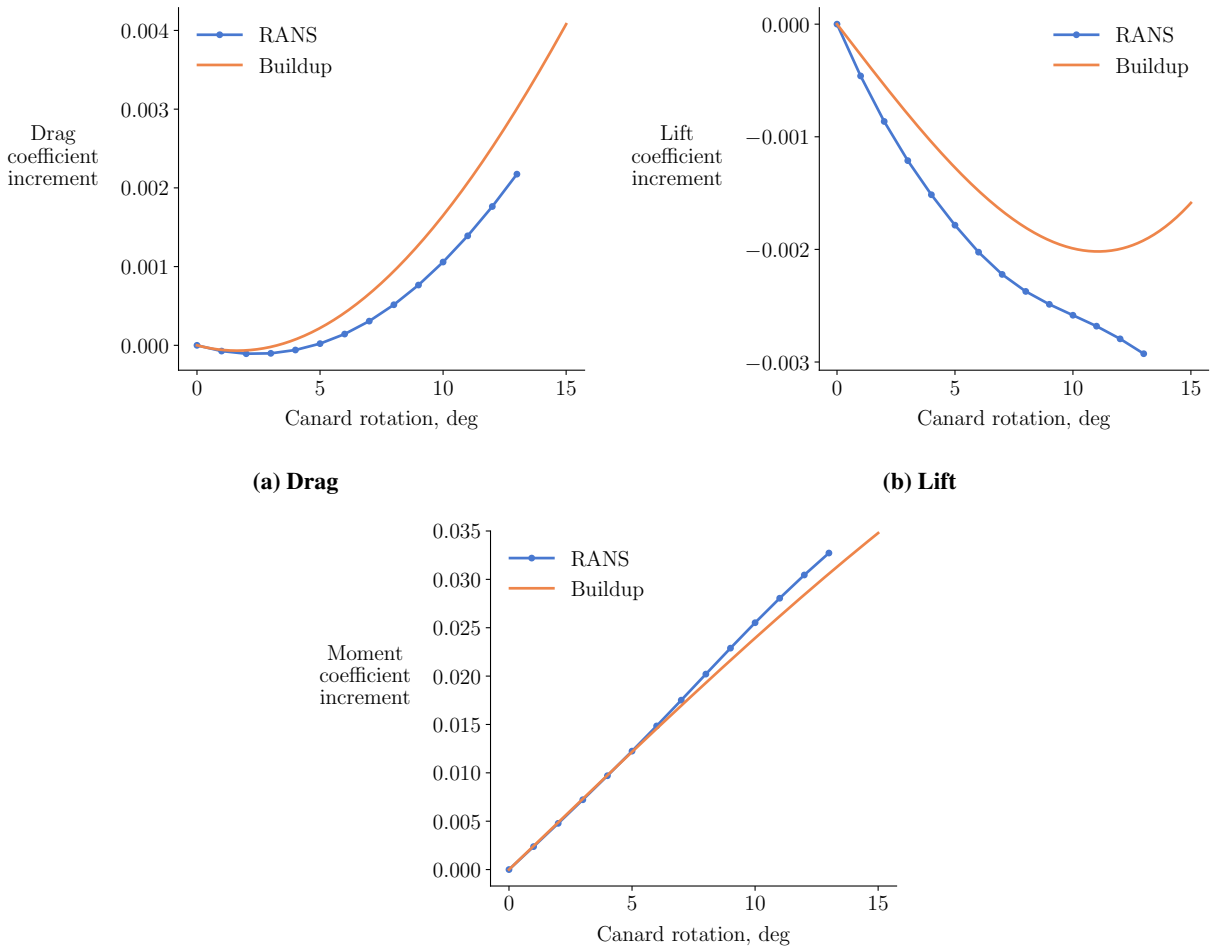


**(a) Drag**

**(b) Lift**

**(c) Pitching moment**

**Fig. 7 Canard rotation increments**

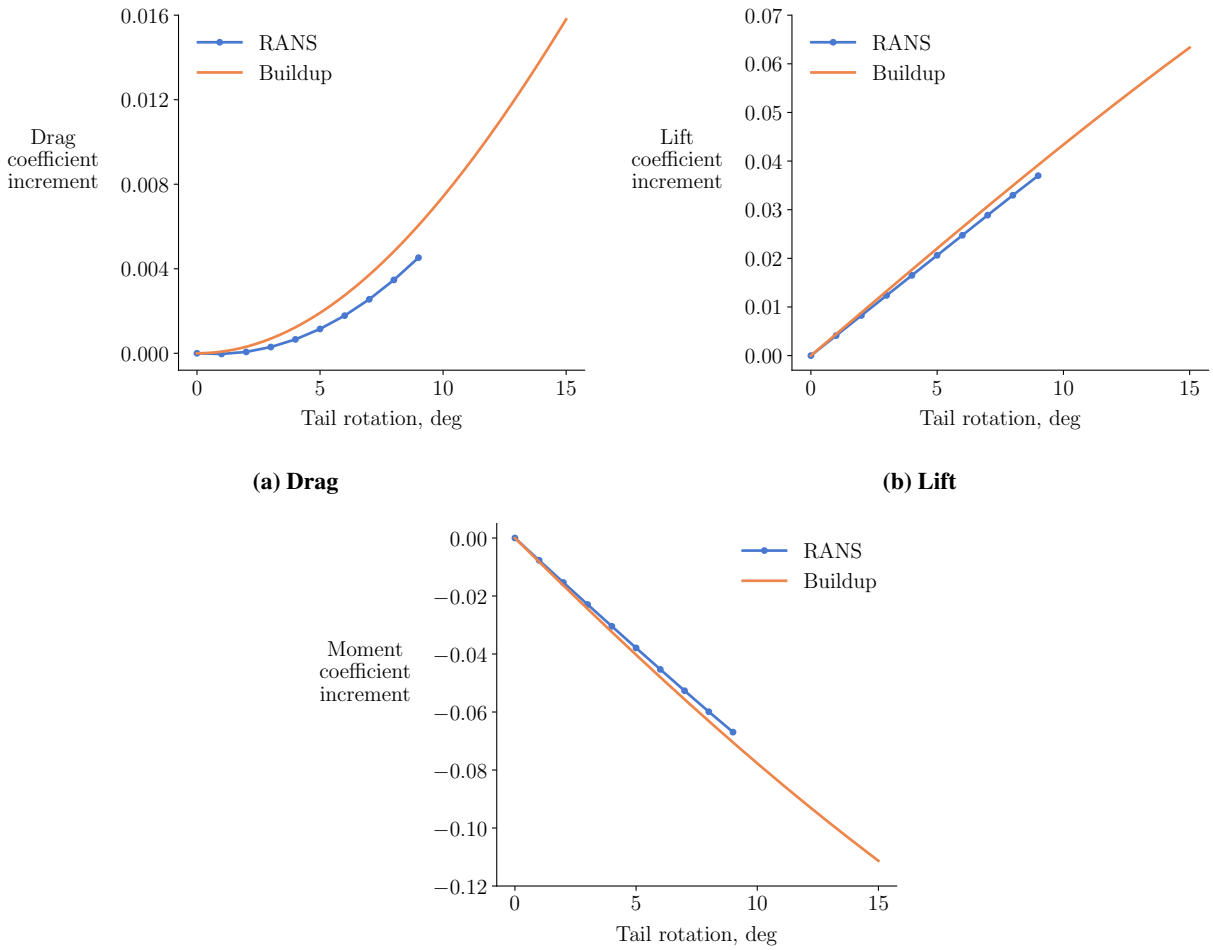


**(a) Drag**

**(b) Lift**

**(c) Pitching moment**

**Fig. 8 Tail rotation increments**

variables is shown in Table 5. We only run buildup-based optimizations for the supersonic condition because the model is not applicable to subsonic flow. Unlike the RANS optimizations, the rotation variables are not bounded by mesh deformation limits. Instead, we bound them to the range where we expect the buildup model to be reasonably accurate. The lower bound for the trim surface span variables is zero. This means that the optimizer has the option of removing either trim surface. Aside from speed, this is the main advantage of using the buildup model in an optimization instead of RANS. Removing a trim surface or doubling its span would not be possible with a mesh deformation approach.

**Table 5 Buildup-based trim surface sizing optimization problem**

| | | Lower | Upper | Scaling |
|---|---|---|---|---|
| Minimize | $C_D$ | | | 10 |
| With respect to | Angle of attack | $-6°$ | $6°$ | 1 |
| | Canard rotation | $-25°$ | $25°$ | 1 |
| | Canard half-span | 0 m | 10 m | 1 |
| | Tail rotation | $-25°$ | $25°$ | 1 |
| | Tail half-span | 0 m | 10 m | 1 |
| Subject to | $C_L$ | 0.1665 | 0.1665 | 1 |
| | $C_M$ | 0 | 0 | 1 |

### C. Buildup-based optimization results

We first use the buildup model to run the same trim-constrained drag minimizations as we did for RANS. These results are presented in Table 4 for ease of comparison with the RANS results. The trimmed buildup drag for the three-surface and conventional configurations match RANS to within 2%. The optimized trim design variables match to within 7%. This provides further verification of the buildup model. The canard configuration optimization is feasible without the mesh-induced upper bound on the canard rotation. The canard configuration has a 37% drag penalty over the three-surface configuration because the canard is stalled to satisfy the trim constraints.

The speed of the buildup model allows us to explore the design space multimodality of the three-surface trim optimization. We run optimizations from 100 random starting points. 96 out of the 100 optimizations converge. We consider the buildup-based optimizations converged when they reach feasibility and optimality values of $10^{-8}$ or lower. These tolerances are much easier to achieve with an analytic model than the RANS equations. All 96 converged optimizations converge to the same design. Figure 9 shows the initial and optimized design variables for the first 20 converged optimizations. This strongly suggests that the optimization problem is unimodal. The unimodality of the three-surface optimization is an important result for aerodynamic shape optimization studies. For shape optimizations, we typically compare the trimmed optimized result with the trimmed baseline configuration [23, 30]. If the trim optimization is unimodal, we can start from any untrimmed state to get the lowest trim drag for the baseline design. This allows for a fair comparison with the trimmed shape optimized design.

Next, we run the trim optimization with span variables. Similar to the previous trim optimization, we run 100 optimizations from different starting points. Unlike the optimization with fixed sizing, this optimization is multimodal. Table 6 shows the best optimized result. The optimized planform has almost no horizontal stabilizer and a canard that is more than twice the span of the baseline (Fig. 10). The canard has a lower lift penalty for a positive moment increment than the tail. Increasing the canard's size allows for trim at a lower angle of attack, which reduces the drag by 10.4% compared to the baseline. One concern with canard designs is that they are more likely to be statically unstable in pitch [31]. We include the static margin for the baseline and optimized designs in Table 6. The static margin is computed as [23]

$$K_n = -\frac{C_{M_\alpha}}{C_{N_\alpha}}, \tag{20}$$

where the derivatives are computed using the complex-step gradients from the optimization. The static margin for the optimized design is lower than the baseline, but the design is still stable.

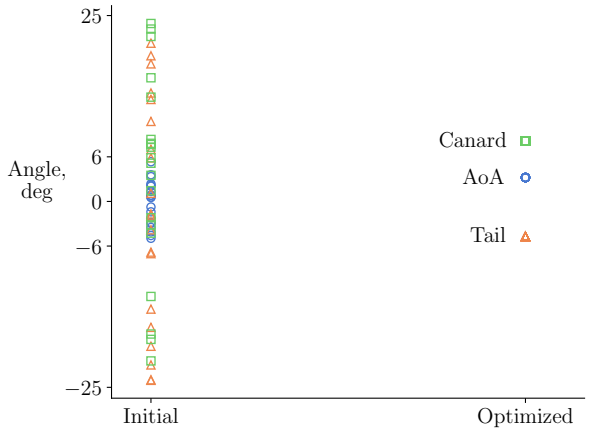


**Fig. 9 The three-surface trim optimization is unimodal**



**(a) Baseline** **(b) Best minimum**

**Fig. 10 Planforms for the trim surface sizing optimization**

**Table 6 Trim surface sizing optimization results**

| | Baseline | Best minimum |
|---|---|---|
| Drag counts | 329.9 | 295.5 |
| Static margin | 23.3% | 6.9% |
| Angle of attack | 3.21° | 2.37° |
| Canard rotation | 8.13° | 7.85° |
| Canard half-span | 2.327 m | 5.280 m |
| Tail rotation | −4.70° | 3.60° |
| Tail half-span | 5.543 m | 0.067 m |

## IV. Conclusions

This work uses nonlinear aerodynamic models and numerical optimization to determine the minimum trim drag configuration for a supersonic transport aircraft. We determine the minimum trim drag for three-surface, canard, and conventional configurations with fixed trim surface sizing using RANS-based optimizations. The three-surface configuration has the lowest trim drag at a supersonic cruise condition. The second best option is the conventional configuration, which has 9.4% higher drag than the three-surface configuration. The canard and three-surface configurations have comparable drag at a subsonic takeoff condition, and the conventional configuration has 11.2% higher drag than the three-surface configuration.

To overcome the mesh-related limitations of the RANS-based optimizations, we formulate a supersonic buildup model. The model is accurate enough to approximate the RANS-based trim optimization results. We also show that the three-surface optimization with fixed sizing is unimodal. We then use the supersonic buildup model to optimize the aircraft with variable trim surface sizing. The design space for this optimization includes the option to remove either trim surface, which would not be possible with an optimization involving mesh deformation. When considering trim surface sizing, the design for minimum supersonic drag has practically no tail and a canard sized at 36% of the wing half-span. These results suggest that a canard configuration can minimize supersonic drag. Further work is required to determine if a canard configuration is still advantageous when also considering subsonic performance and stability.

## Acknowledgments

This work was supported by NASA's Commercial Supersonic Technology project. S. Seraj was also supported by the Natural Sciences and Engineering Research Council of Canada (funding reference number PGSD3-545678-2020). Computational resources were provided by the NASA High-End Computing Program through the NASA Advanced Supercomputing Division at Ames Research Center. The MACH framework, co-invented by Joaquim Martins, is used by Supercritical Research, LLC, a company owned by Joaquim Martins.

## References

[1] Kendall, E. R., "The theoretical minimum induced drag of three-surface airplanes in trim," *Journal of Aircraft*, Vol. 22, No. 10, 1985, pp. 847–854. doi:10.2514/3.45214.

[2] Kroo, I., "A General Approach to Multiple Lifting Surface Design and Analysis," *Aircraft Design Systems and Operations Meeting*, 1984. doi:10.2514/6.1984-2507.

[3] Selberg, B. P., and Rokhsaz, K., "Aerodynamic Tradeoff Study of Conventional, Canard, and Trisurface Aircraft Systems," *Journal of Aircraft*, Vol. 23, No. 10, 1986, pp. 768–774. doi:10.2514/3.45379.

[4] Rokhsaz, K., and Selberg, B. P., "Three-Surface Aircraft – Optimum vs Typical," *Journal of Aircraft*, Vol. 26, No. 8, 1989, pp. 699–704. doi:10.2514/3.45827.

[5] Lacey, D. W., "Aerodynamic Characteristics of the Close-Coupled Canard as Applied to Low-to-Moderate Swept Wings. Volume 3. Transonic-Supersonic Speed Regime," Tech. rep., Naval Ship Research and Development Center, Bethesda, Maryland, USA, 1979.

[6] Agnew, J. W., and Hess Jr., J. R., "Benefits of Aerodynamic Interaction to the Three-Surface Configuration," *Journal of Aircraft*, Vol. 17, No. 11, 1980, pp. 823–827. doi:10.2514/3.57971.

[7] Covell, P. F., "Supersonic Aerodynamic Characteristics of Canard, Tailless, and Aft-Tail Configurations for Two Wing Planforms," Tech. Rep. NASA-TP-2434, NASA Langley Research Center, Hampton, Virginia, USA, 1985.

[8] Candel, S., "Concorde and the Future of Supersonic Transport," *Journal of Propulsion and Power*, Vol. 20, No. 1, 2004, pp. 59–68. doi:10.2514/1.9180.

[9] Nelson, C. P., Ting, K.-Y., Mavriplis, N., Soltani, R., and Livne, E., "Supersonic Configurations at Low Speeds (SCALOS): Project Background and Progress at University of Washington," *AIAA SciTech Forum*, 2022. doi:10.2514/6.2022-1803.

[10] Welge, H. R., Bonet, J., Magee, T., Chen, D., Hollowell, S., Kutzmann, A., Mortlock, A., Stengle, J., Nelson, C., Adamson, E., Baughcum, S., Britt, R. T., Miller, G., and Tai, J., "N+2 Supersonic Concept Development and Systems Integration," Tech. Rep. NASA/CR-2010-216842, NASA, Langley Research Center, Hampton, VA, 2010.

[11] Morgenstern, J., Buonanno, M., Yao, J., Murugappan, M., Paliath, U., Cheung, L., Malcevic, I., Ramakrishnan, K., Pastouchenko, N., Wood, T., Martens, S., Viars, P., Tersmette, T., Lee, J., Simmons, R., Plybon, D., Alonso, J., Palacios, F., Lukaczyk, T., and Carrier, G., "Advanced Concept Studies for Supersonic Commercial Transports Entering Service in the 2018-2020 Period Phase 2," Tech. Rep. NASA/CR—2015-218719, NASA, Glenn Research Center, Cleveland, OH, 2015.

[12] Martins, J. R. R. A., "Aerodynamic Design Optimization: Challenges and Perspectives," *Computers & Fluids*, Vol. 239, 2022, p. 105391. doi:10.1016/j.compfluid.2022.105391.

[13] Mader, C. A., Kenway, G. K. W., Yildirim, A., and Martins, J. R. R. A., "ADflow: An open-source computational fluid dynamics solver for aerodynamic and multidisciplinary optimization," *Journal of Aerospace Information Systems*, Vol. 17, No. 9, 2020, pp. 508–527. doi:10.2514/1.I010796.

[14] Spalart, P., and Allmaras, S., "A One-Equation Turbulence Model for Aerodynamic Flows," *La Recherche Aerospatiale*, Vol. 1, 1994, pp. 5–21.

[15] Yildirim, A., Mader, C. A., and Martins, J. R. R. A., "A Surface Mesh Deformation Method Near Component Intersections for High-Fidelity Design Optimization," *Engineering with Computers*, 2021. doi:10.1007/s00366-020-01247-w.

[16] Sederberg, T. W., and Parry, S. R., "Free-form Deformation of Solid Geometric Models," *SIGGRAPH Comput. Graph.*, Vol. 20, No. 4, 1986, pp. 151–160. doi:10.1145/15886.15903.

[17] Kenway, G. K., Kennedy, G. J., and Martins, J. R. R. A., "A CAD-Free Approach to High-Fidelity Aerostructural Optimization," *Proceedings of the 13th AIAA/ISSMO Multidisciplinary Analysis Optimization Conference*, Fort Worth, TX, 2010. doi:10.2514/6.2010-9231.

[18] Luke, E., Collins, E., and Blades, E., "A Fast Mesh Deformation Method Using Explicit Interpolation," *Journal of Computational Physics*, Vol. 231, No. 2, 2012, pp. 586–601. doi:10.1016/j.jcp.2011.09.021.

[19] Secco, N., Kenway, G. K. W., He, P., Mader, C. A., and Martins, J. R. R. A., "Efficient Mesh Generation and Deformation for Aerodynamic Shape Optimization," *AIAA Journal*, Vol. 59, No. 4, 2021, pp. 1151–1168. doi:10.2514/1.J059491.

[20] Gill, P. E., Murray, W., and Saunders, M. A., "SNOPT: An SQP Algorithm for Large-Scale Constrained Optimization," *SIAM Review*, Vol. 47, No. 1, 2005, pp. 99–131. doi:10.1137/S0036144504446096.

[21] Wu, N., Kenway, G., Mader, C. A., Jasa, J., and Martins, J. R. R. A., "pyOptSparse: A Python framework for large-scale constrained nonlinear optimization of sparse systems," *Journal of Open Source Software*, Vol. 5, No. 54, 2020, p. 2564. doi:10.21105/joss.02564.

[22] Kenway, G. K. W., Mader, C. A., He, P., and Martins, J. R. R. A., "Effective Adjoint Approaches for Computational Fluid Dynamics," *Progress in Aerospace Sciences*, Vol. 110, 2019, p. 100542. doi:10.1016/j.paerosci.2019.05.002.

[23] Seraj, S., and Martins, J. R. R. A., "Aerodynamic Shape Optimization of a Supersonic Transport Considering Low-Speed Stability," *AIAA SciTech Forum*, 2022. doi:10.2514/6.2022-2177.

[24] Raymer, D. P., *Aircraft Design: A Conceptual Approach*, 5$^{\text{th}}$ ed., AIAA, Reston, VA, 2012.

[25] Tangler, J. L., and Ostowari, C., "Horizontal axis wind turbine post stall airfoil characteristics synthesization," Conference paper presented at the DOE/NASA Wind Turbine Technology Workshop, May 1984. In Collected Papers on Wind Turbine Technology, NASA-CR-195432, May 1995.

[26] Chauhan, S. S., and Martins, J. R. R. A., "Tilt-wing eVTOL takeoff trajectory optimization," *Journal of Aircraft*, Vol. 57, No. 1, 2020, pp. 93–112. doi:10.2514/1.C035476.

[27] Kreisselmeier, G., and Steinhauser, R., "Systematic Control Design by Optimizing a Vector Performance Index," *International Federation of Active Controls Symposium on Computer-Aided Design of Control Systems, Zurich, Switzerland*, 1979. doi:10.1016/S1474-6670(17)65584-8.

[28] Gray, J. S., Hwang, J. T., Martins, J. R. R. A., Moore, K. T., and Naylor, B. A., "OpenMDAO: An open-source framework for multidisciplinary design, analysis, and optimization," *Structural and Multidisciplinary Optimization*, Vol. 59, No. 4, 2019, pp. 1075–1104. doi:10.1007/s00158-019-02211-z.

[29] Martins, J. R. R. A., Sturdza, P., and Alonso, J. J., "The Complex-Step Derivative Approximation," *ACM Transactions on Mathematical Software*, Vol. 29, No. 3, 2003, pp. 245–262. doi:10.1145/838250.838251.

[30] Chen, S., Lyu, Z., Kenway, G. K. W., and Martins, J. R. R. A., "Aerodynamic Shape Optimization of the Common Research Model Wing-Body-Tail Configuration," *Journal of Aircraft*, Vol. 53, No. 1, 2016, pp. 276–293. doi:10.2514/1.C033328.

[31] Torenbeek, E., *Essentials of Supersonic Commercial Aircraft Conceptual Design*, John Wiley & Sons Ltd., 2020. doi:10.1002/9781119667063.